

Article

A New Zincian Greenockite Occurrence in the Saishitang Cu Skarn Deposit, Qinghai Province, Northwest China

Jianping Liu and Shugen Zhang *

Key Laboratory of Metallogenic Prediction of Non-Ferrous Metals and Geological Environment Monitor (Central South University), Ministry of Education, Changsha 410083, China; liujianping@csu.edu.cn

* Correspondence: zhangshugenzsg@163.com; Tel.: +86-731-888-30616

Received: 15 June 2017; Accepted: 26 July 2017; Published: 28 July 2017

Abstract: Zn-Cd-S series minerals not only comprise industrial resources for Zn and Cd, but are also significant mineralogical indicators for hydrothermal ore-forming processes. Due to its unique formation conditions and rare occurrence, our understanding of the formation of zincian greenockite in natural systems is limited. Zincian greenockite was discovered during mineralogical studies in the Saishitang Cu skarn deposit, Qinghai Province, Northwest China. This provided an ideal opportunity to assess the occurrence and formation of zincian greenockite in skarn-type deposits. Ore minerals were observed using reflected-light microscopy, and the zincian greenockite was further analyzed using electron-probe microanalysis (EPMA) and X-ray diffraction (XRD). The zincian greenockite occurs in the bornite–chalcopyrite ores and is composed of subhedral to anhedral grains approximately $50 \times 150 \mu\text{m}^2$ to $200 \times 300 \mu\text{m}^2$ in size, replaces the bornite, and is replaced by native silver. Two phases (I and II) were identified based on back-scattered electron images, X-ray element-distributions maps, and EPMA data. The textural relationship indicated that Phase I was replaced by Phase II. Phase I contained high Zn (14.6 to 21.7 mol % ZnS) and low Cd (72.4 to 82.2 mol % CdS), while Phase II contained low Zn (5.6 to 9.1 mol % ZnS) and high Cd (85.4 to 89.9 mol % CdS). The zincian greenockite was formed at temperature of 300–270 °C during the transformation from a reducing environment to an oxidizing one in the late stage of the mineralization process in the Saishitang deposit.

Keywords: zincian greenockite; copper skarn deposit; Saishitang; Northwest China

1. Introduction

The Zn-Cd-S component system is of theoretical and practical significance for mineralogy and materials science [1–3]. There are two structure types (cubic and hexagonal) for this system; the end members of ZnS and CdS are sphalerite and wurtzite, and hawleyite and greenockite, respectively. Sphalerite is one of the most common ore minerals, while wurtzite and greenockite are much less abundant, and hawleyite is rare [2]. Experimental studies of the system ZnS-CdS have indicated the existence of a complete solid solution at temperatures above 600 °C [4–10]. It has been shown that the solid solution exists to an extent at hydrothermal conditions below 400 °C [4], and that the replacement of Cd by Zn is a rather complicated process that is dependent on the formation environment [11].

Greenockite is formed predominantly as a weathering product of Cd-bearing sphalerite [11]. However, greenockite also occurs as a primary mineral in various geological settings [4,11,12], including (i) pegmatites [13], (ii) granites [14], (iii) fumaroles [2], (iv) chromite-PGE mineralization [12], (v) hydrothermal ore deposits [4,11], (vi) estuarine sediments [15,16], and (vii) shales [17]. The predominant occurrences of greenockite in hydrothermal deposits are in Pb-Zn deposits, such as sediment-hosted Pb-Zn deposits [18,19], volcanic-related Pb-Zn deposits [20–22], as well as a few in

orogenic Au deposits [23] and epithermal Au-Ag deposits [4,24]. Its existence is yet to be reported in skarn deposits.

The Saishitang deposit is an important deposit with metal reserves of 0.43 Mt Cu [25] in Qinghai Province, Northwest China. The deposit is hosted in stratiform skarn, which contains 1468 t of Cd, last evaluated in 1980s [25]. Zincian greenockite was previously discovered during critical metals studies [26]. This provides a good opportunity to assess how the zincian greenockite was formed during the mineralization processes of skarn deposits. In this paper, mineralogical investigations for ores of the Saishitang Cu deposit were first performed, after which the mineral chemistry and unit-cell parameters of the zinc greenockite were obtained. Finally, the forming conditions of the zincian greenockite were discussed.

2. Geological Setting

2.1. Regional Geology of the Elashan Region

The Saishitang deposit is situated in the Elashan Metallogenic Belt (EMB) [27], Qinghai Province, Northwest China (Figure 1a). Geodynamically, the EMB is located in the junction between the western Qinling orogenic belt and eastern Kunlun orogenic belt [28,29]. The lithologies of the EMB are composed of the Paleoproterozoic Jingshuikou Group gneisses, Ordovician to Carboniferous volcanic and carbonate rocks, Lower Permian carbonate and clastic rocks, Triassic carbonate and volcanoclastic rocks, and Neogene glutenite and Quaternary soil (Figure 1b).

The EMB experienced multiple periods of granitic magmatism from the Proterozoic to Early Mesozoic (Figure 1b) [30]. The dominant periods are marked by Ordovician-Silurian (Variscan) and Permian-Triassic (Indosinian) units [28,30,31], with Late Triassic granites [30] being most abundant in the EMB. The Late Triassic granites are I-type granites with minor A-type granites, which are believed to have been generated during the post-collision orogenic stage [31,32].

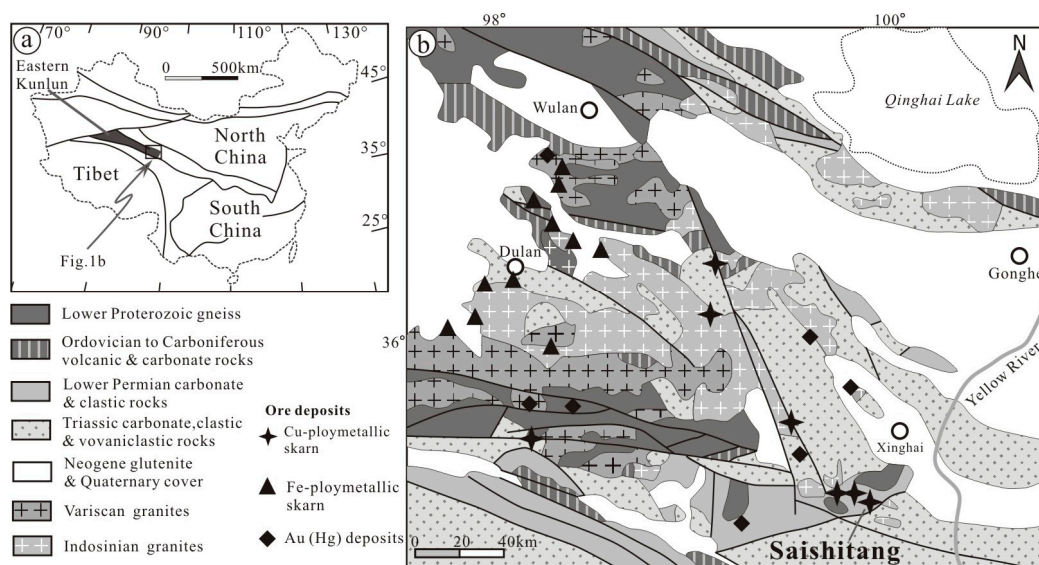


Figure 1. (a) Tectonic maps indicating the location of the Elashan Region, Northwest (NW) China; (b) Simplified geological map and skarn deposits of the Elashan Region (after Refs. [33,34]).

A large number of Cu-polymetallic skarn, Fe-polymetallic skarn, and orogenic Au deposits (Figure 1b) in the EMB are related to the Late Triassic granites [34]. Cu-polymetallic skarn deposits are distributed east of the Elashan region, particularly in the Saishitang-Rilonggou orefield [26,29,35] which is the most important Cu mineralization area in Qinghai, or even in China [35]. Among these deposits,

the Saishitang Cu deposit is a well-developed and studied deposit [26–29,36,37], and furthermore, constitutes a typical skarn Cu deposit example for understanding mineralization in the Elashan region.

2.2. Geology of the Saishitang Cu Deposit

2.2.1. Stratigraphy

The stratigraphy of the Saishitang deposit consists mainly of a Lower Permian series that underwent extensive regional metamorphism (also regarded as the Middle-Lower Triassic by some researchers [28]) overlain by Paleogene-Neogene and Quaternary covers (Figure 1b), as well as a slice of Proterozoic high-grade metamorphosed rock [26,29]. The ore-bearing stratum of the Saishitang deposit constitutes Group C of the Lower Permian series [26]. Skarn and ore bodies occur mainly in the contact between intrusions, metamorphosed tuff, and marble-containing metamorphosed siltstone [28].

2.2.2. Intrusive Rocks

The complex intrusions of the Saishitang deposit outcrop on a northwest-southeast (NW-SE) strike and are 3.5 km long and 0.5–1 km wide. Five intrusions were previously outlined (named I, II, III, IV, V) [38]. The intrusions are complex, comprising five stages (stages A, B, C, D, E), and were identified based on crosscutting relationships and petrologic features. Stage A consists of diorite dykes distributed in the west of the No. III intrusion. Stage B constitutes medium-grained quartz diorite distributed in intrusions I and IV. Stage C is composed of fine-grained quartz diorite, plagioclase granite, and granodiorite porphyry, and is distributed in intrusions II and III. Stage D constitutes intermediate-felsic dykes, and Stage E is composed of felsic dykes [38]. According to the alteration features, Stages A and B are pre-mineralization intrusions; Stage C is a syn-mineralization intrusion, and Stages D and E are post-mineralization intrusions. Geochemical and mineralogical features indicate that the intrusions are I-type granites [28]. The Hf isotope data indicates that the intrusions of the Saishitang deposit originated from the partial melting of Mesoproterozoic lower crustal materials with the involvement of mantle-derived magmas [28]. The zircon U-Pb ages of the quartz diorite yielded an estimate of 223–220 Ma, suggesting that they were emplaced in the Late Triassic [26,39].

2.2.3. Orebodies

The Saishitang deposit contains a total of 176 orebodies including Cu, Pb-Zn, and Fe orebodies, and the three largest orebodies are named M2, M1, and M4 (Figure 2b,c) [25,40]. The M2 orebody (Figure 2c), constituting the biggest orebody in the deposit, exceeds 2500 m in length and is typically 5–15 m thick (locally up to 39 m thick), and has an ore grade of 0.36–3.63 wt % copper (average 1.07 wt %) [27]. The orebodies hosted in the stratiform skarn occur between the marble and meta-siltstone or phyllite, and are stratoid, lenticular, and NW-trending and southwest (SW) dipping (Figure 2b,c) [28].

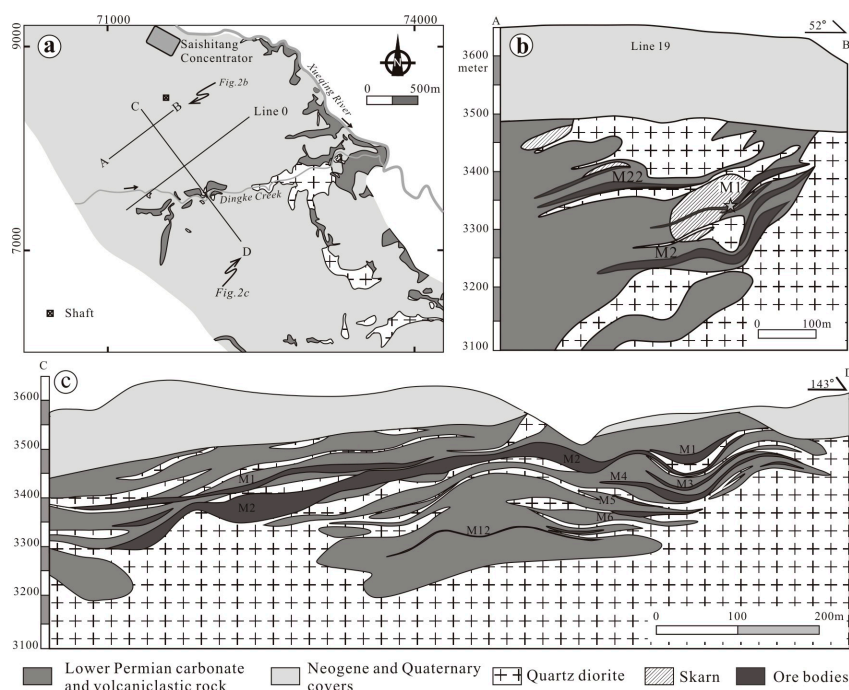


Figure 2. (a) Geological map; (b) cross section of Line 19; and (c) C-D section of the Saishitang Cu deposit (after [26]).

2.2.4. Ore Types and Mineral Paragenetic Sequence

The ore minerals are composed of chalcopyrite, magnetite, pyrrhotite, and pyrite, with galena, sphalerite, arsenopyrite, bornite, and the following trace minerals: wittichenite, stromeyerite, native silver, and native bismuth. Gangue minerals include diopside, garnet, wollastonite, amphibole, epidote, chlorite, quartz, and calcite. Based on the ore mineral assemblages, the ores can be divided into five main sub-types: magnetite-chalcopyrite ores, pyrrhotite-chalcopyrite ores, pyrite-chalcopyrite ores, chalcopyrite-bornite ores, and metasiltite-hosted chalcopyrite ores [27]. The zincian greenockite is hosted in the chalcopyrite-bornite ores (Figure 3).

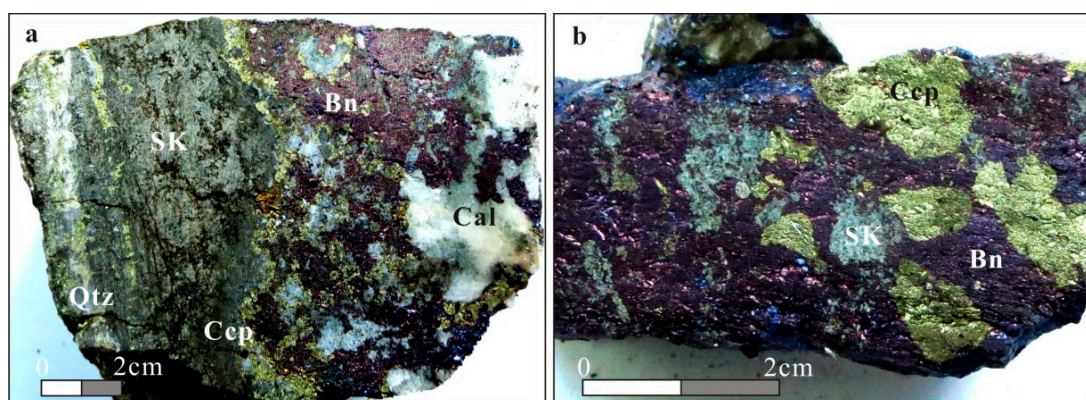


Figure 3. Photographs of bornite-chalcopyrite ore samples containing the zincian greenockite of the Saishitang Cu deposit. (a) Hand specimen of skarn-hosted ore, with bornite (Bn), chalcopyrite (Ccp), skarn minerals (SK), quartz (Qtz), and calcite (Cal); (b) massive ore, with chalcopyrite in the bornite. Note the subrounded boundaries of the chalcopyrite.

Field and textural relationships indicate that the skarn- and ore-forming processes can be divided into two periods and six stages, including: (1) the skarn period, which includes an anhydrous skarn

stage (Stage I) and a hydrous skarn stage (Stage II); and (2) the hydrothermal period, including a magnetite stage (Stage III), a first sulfide stage (Stage IV), a second sulfide stage (Stage V), and a sulfide-sulfosalt stage (Stage VI). The paragenetic sequence of the Saishitang deposit is shown in Figure 4.

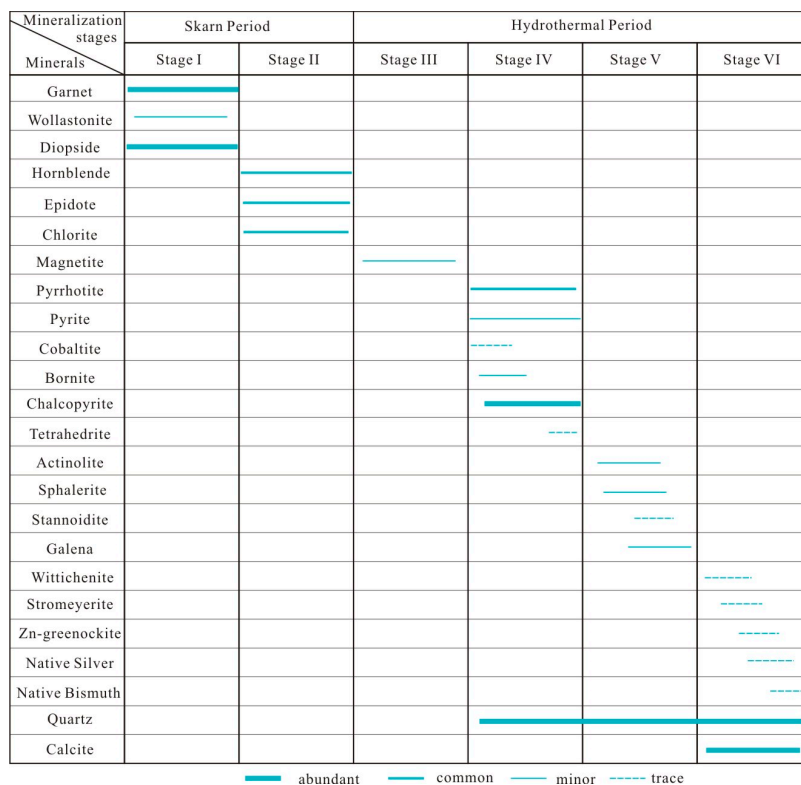


Figure 4. Paragenetic sequence of the Saishitang Cu deposit.

The skarn period is characterized by the precipitation of anhydrous skarn minerals such as grossular-andradite garnet [41], diopside, and wollastonite (Stage I), which are replaced by the hydrous skarn minerals, such as amphibole and epidote (Stage II).

The hydrothermal period can be divided into four stages. Stage III is characterized by the precipitation of the magnetite, replacing the garnet (Figure 5a). Minerals formed at Stage IV mostly include pyrite and chalcopyrite, bornite (Figure 5b), and pyrrhotite. The cobaltite is euhedral-subhedral, and is replaced by chalcopyrite and tetrahedrite (Figure 5c,d). The bornite is replaced by chalcopyrite and tetrahedrite (Figure 5c), while the chalcopyrite shows a leaf-like texture in the bornite (Figure 5g) or replaced bornite (Figure 5c). Minerals formed at Stage V include sphalerite, stannoidite, galena, actinolite, and quartz. Stannoidite replaces the bornite (Figure 5h). Minerals formed at Stage VI include wittichenite, stromeyerite, zincian greenockite, native silver, native bismuth, quartz, and calcite. Wittichenite and stromeyerite fill the fractures of the bornite, and the native silver and native bismuth replace the stromeyerite (Figure 5e,f). The detailed texture of the zincian greenockite is described in Section 4.1.

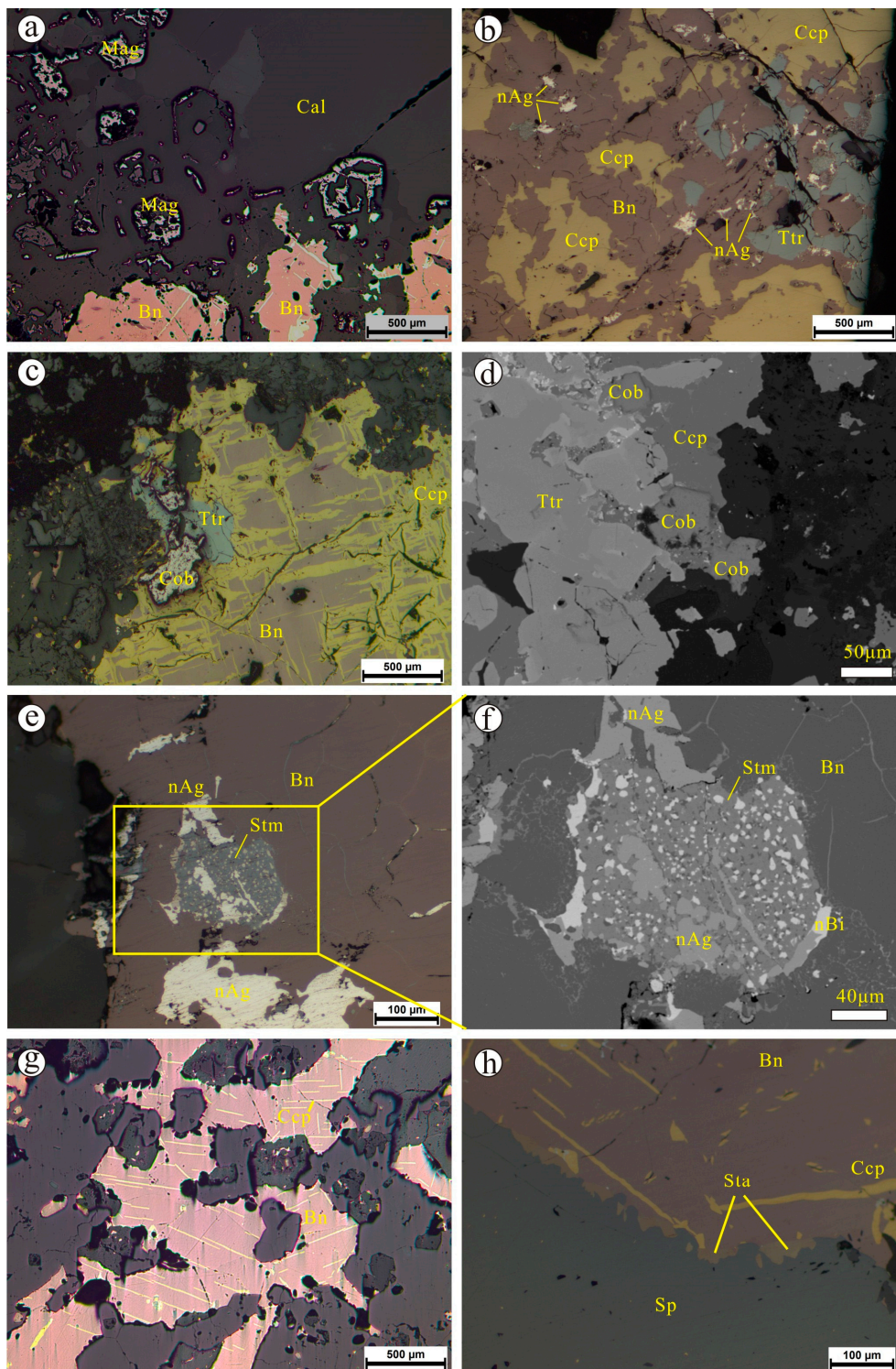


Figure 5. Reflected light (a–c,e,g,h) and backscattered electron images (d,f) showing textural relations of ore minerals. (a) Magnetite (Mt) replaces garnet (Grt), and filled by calcite (Cal); (b) bornite (Bn) replaces tetrahedrite (Ttr), and replaced by chalcopyrite (Ccp), with native silver (nAg) filling the fracture; (c) tetrahedrite replacing the chalcopyrite, chalcopyrite replacing the bornite, and cobaltite (Cob) replaced by tetrahedrite, chalcopyrite, and bornite; (d) cobaltite is subhedral to anhedral and replaced by chalcopyrite and tetrahedrite; (e) stromeyerite fills bornite, and is filled by native silver and native bismuth (nBi); (f) enlarged image of Figure 5e showing native silver and native bismuth fill stromeyerite (Stm), with native bismuth occurring later than native silver; (g) leaf-like texture of chalcopyrite in bornite; (h) stannoidite (Sta) occurring between bornite and sphalerite.

3. Sampling and Analytical Methods

3.1. Sampling Site

In our previous study [26], 19 ore samples were collected from 3400, 3350, 3300, and 3250 m above sea level (a.s.l) from underground workings and ores stores of the Saishitang deposit. The bornite-chalcopyrite ores that contain zincian greenockite were obtained from Line 19 at 3300 m a.s.l, and Line 18 at 3350 m a.s.l.

3.2. Electron-Probe Microanalyses

The ore minerals and textures were identified in polished thick sections using standard reflected-light microscopy techniques. The mineral chemical compositions and X-ray mapping were analyzed using a Shimadzu EPMA-1720H (Tokyo, Japan) electron probe micro-analyzer (EPMA) housed at the School of Geosciences and Info-physics (SGI), Central South University (CSU), Changsha, China. The operating conditions of the electron microprobe included a 15 kV accelerating voltage, 10 nA beam current, and 1 μm diameter electron beam. The X-ray lines used to analyze the different elements were as follows: S ($K\alpha$), Mn ($K\alpha$), Fe ($K\alpha$), Cu ($K\alpha$), Zn ($K\alpha$), Ag ($L\alpha$), and Cd ($L\alpha$). The mineral and metal standards used for elemental calibration included pyrite (S), metallic Mn (Mn), pyrite (Fe), chalcopyrite (Cu), sphalerite (Zn), argentite (Ag), and greenockite (Cd). The resulting data were processed by the atomic number (Z), absorption (A) and fluorescence (F) effects (ZAF) correction method using proprietary Shimadzu software.

3.3. X-ray Diffraction Analysis

X-ray diffraction (XRD) analysis was performed with a Rigaku D/Max Rapid IIR microdiffractometer (Rigaku Corporation, Tokyo, Japan) at 40 kV and 250 mA, using a Cu tube and a 0.05 mm collimator with 20 min exposure. The XRD raw data were processed using Jade 6.0 software, and recorded from 20° to 60° 2θ . The peaks were matched using the Powder Diffraction File (PDF) of the International Centre for Diffraction Data. The XRD analysis was completed at the SGI, CSU, Changsha, China.

4. Results

4.1. Optical Properties and Textural Relations for Zincian Greenockite

In reflected light micrographs, zincian greenockite featured as dark grey, with low reflectance (but higher than sphalerite), weak anisotropism, and salmon to yellow internal reflection. Zincian greenockite was harder than bornite (Figure 6a) and the grains were subhedral to anhedral (Figure 6), approximately $50 \times 150 \mu\text{m}^2$ to $200 \times 300 \mu\text{m}^2$, and occurred on the edges of the chalcopyrite, quartz, and calcite. Texturally, the bornite was replaced by the zincian greenockite later than the actinolite, which was replaced by the native silver (Figure 6).

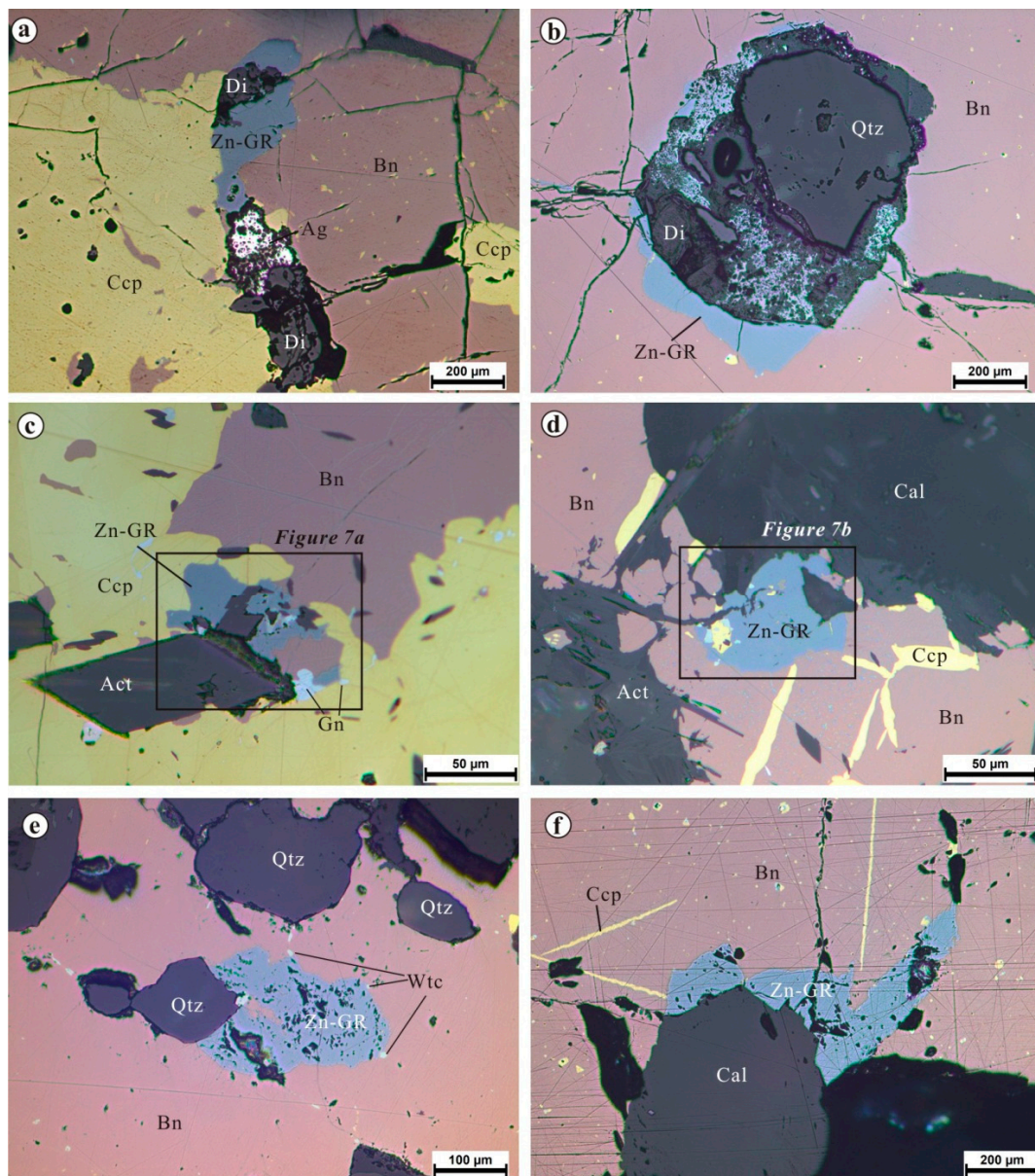


Figure 6. Reflected light photomicrographs of zincian greenockite. (a) zincian greenockite (Zn-GR), native silver (Ag), and diopside (Di) between chalcopyrite (Ccp) and bornite (Bn) grains; (b) zincian greenockite occurs in the contacts between bornite and diopside (Di) and quartz (Qtz); (c) zincian greenockite as a subrounded grain at the margin of the chalcopyrite associated with actinolite (Act) and galena (Gn) (the detailed back-scattered electron (BSE) images can be observed in Figure 7a); (d) zincian greenockite at the contact between bornite and actinolite (the detailed BSE image can be observed in Figure 7b); (e) zincian greenockite with wittichenite (Wtc) filling and replacing the bornite; (f) zincian greenockite filling in the fractures of bornite, and its association with calcite (Cal).

4.2. Composition of Zincian Greenockite and Associated Minerals

4.2.1. Zincian Greenockite

A total of 30 spots were analyzed on six grains (No.: k31a5, k31a6, k31b, k31.6, k31b.15, and k31b.16; Table 1) of two samples (k31a, and k31b). The spots were selected with the assistance of X-ray maps. Examples of the Zn and Cd X-ray maps of the single grains are provided in Figure 7.

Zincian greenockite contained 62.53 to 72.66 wt % Cd, 2.66 to 10.88 wt % Zn, and 22.77 to 25.05 wt % S, with small amounts of Cu (0.06 to 2.39 wt %) and Fe (0.07 to 0.76 wt %), as well as traces of Ag (<0.01 to 0.08 wt %) and Mn (<0.01 to 0.09 wt %). The Cd/(Cd+Zn) ratios ranged from 0.77 to 0.94 (Figure 8). Two phases of zincian greenockite were identified by the BSE images and X-ray mapping of Zn and Cd (Figures 7 and 9), including: Phase I with high Zn (14.6 to 21.7 mol % ZnS) and low Cd (72.4 to 82.2 mol % CdS), and Phase II with low Zn (5.6 to 9.1 mol % ZnS) and high Cd (85.4 to 89.9 mol % CdS).

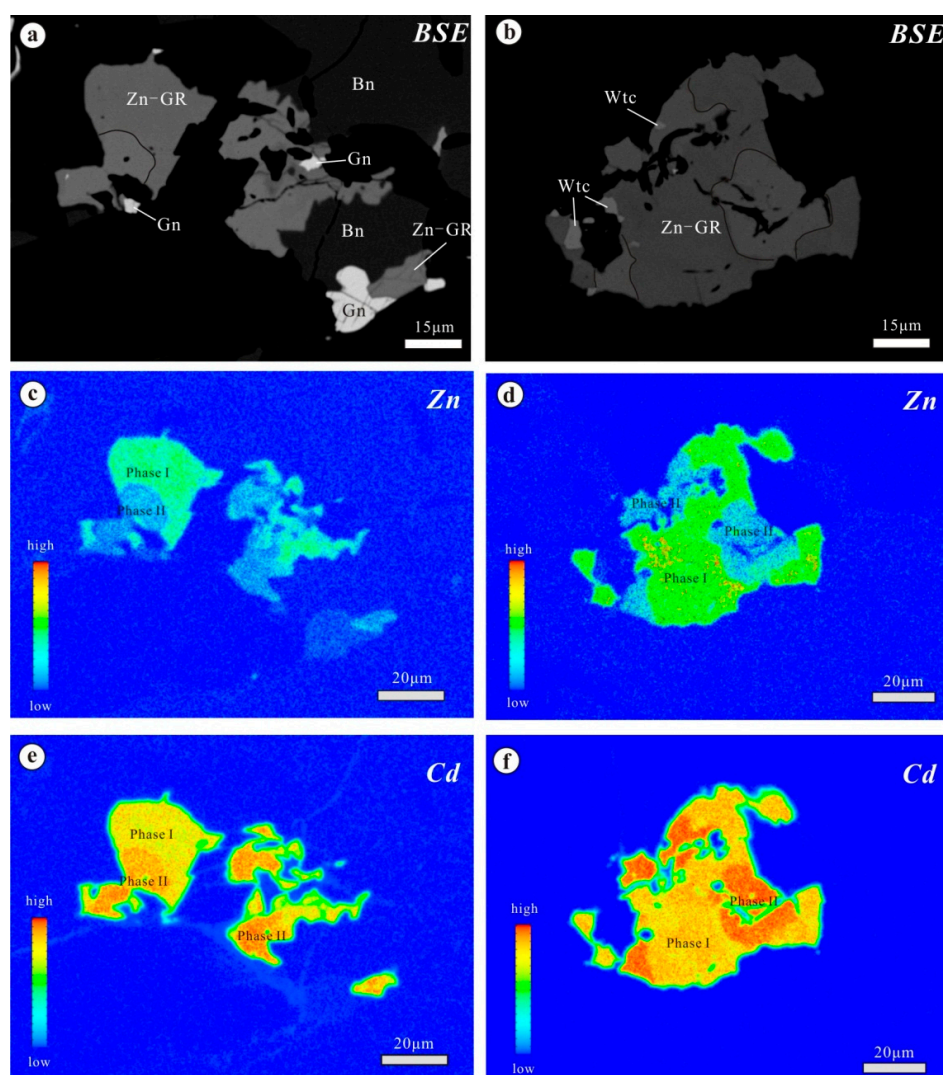


Figure 7. (a,b) Back-scattered electron images (BSE) of zincian greenockite; (c,e) X-ray element-distribution maps for Zn and Cd of zincian greenockite for the area shown in Figure 6d; (d,f) X-ray element-distribution maps for Zn and Cd of zincian greenockite for the area of Figure 6c. The two grains indicate that the distribution of Zn and Cd is inhomogeneous and demonstrate an inverse correlation between Zn and Cd in zincian greenockite. Two phases (I and II) are evident and discussed in the text. Mineral abbreviations: Zn-GR = zincian greenockite, Bn = bornite, Wtc = wittichenite, Gn = galena.

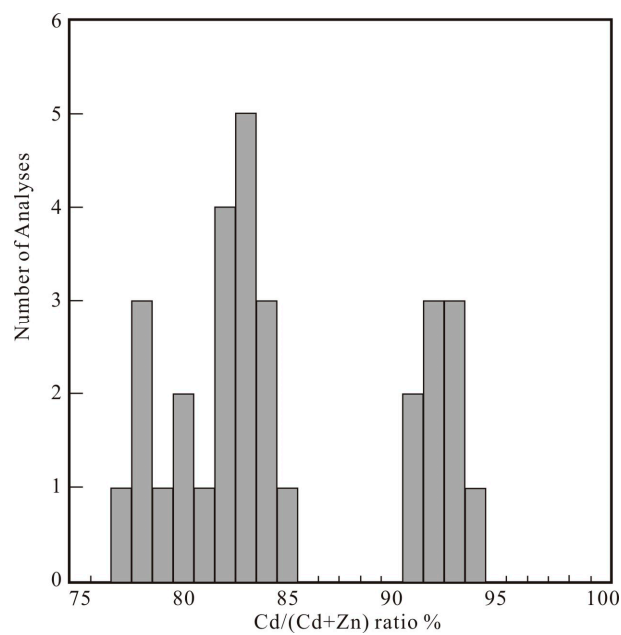


Figure 8. Histogram of the Cd/(Cd+Zn) ratio of zincian greenockite of the Saishitang deposit.

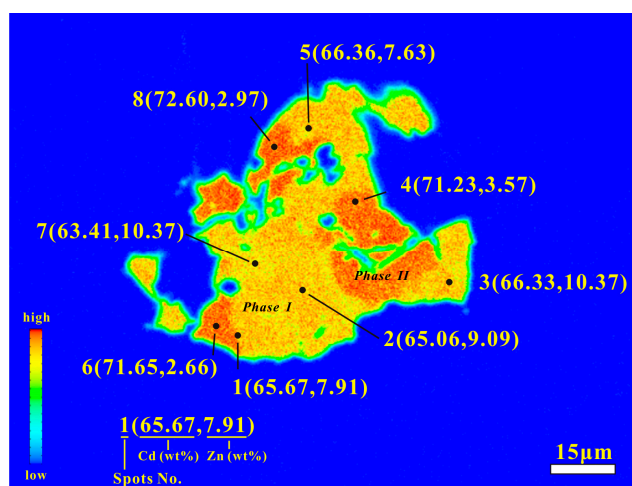


Figure 9. Enlargement of Figure 7f showing the electron-probe microanalysis data of Cd and Zn in Phase I and Phase II of zincian greenockite. Spots 1, 2, 3, 5, & 7 are from Phase I (light yellow areas) and possess less than 67 wt % Cd, and spots 4, 6, & 8 are from Phase II (dark red areas) and possess more than 71 wt % Cd.

Table 1. EPMA data and atomic proportions of zincian greenockite. n/a: not analyzed; n/d: not detected; apfu: atoms per formula unit.

Sample	1k31a.5				1k31a.6				k31b.5				k31b.6	k31b.15		
	1	3	4	5	1	2	3	4	e	d	c	h	f	c	1	
	wt %															
Cd	64.82	68.4	64.9	68.27	64.78	66.89	67.04	63.51	62.53	63.31	70.08	71.71	70.85	65.5	65.67	
Zn	8.41	7.08	9.29	7.29	9.54	7.93	7.67	10.26	10.88	10.31	3.48	3.01	3.46	7.59	7.91	
Cu	1.28	0.06	0.44	0.12	0.20	0.14	0.20	0.34	1.92	1.48	2.39	0.69	1.83	0.61	2.07	
Fe	0.26	0.07	0.16	0.12	0.13	0.17	0.09	0.20	0.76	0.44	0.43	0.53	0.48	0.17	0.38	
Mn	0.01	0.06	0.06	0.09	n/d	n/d	0.03	n/d	0.02	0.06	0.04	0.09	0.03	0.07	n/d	
Ag	n/a	n/a	n/a	n/a	n/a	n/a	n/a	n/a	0.04	0.05	0.08	0.01	0.07	0.03	n/d	
S	24.4	24.43	24.33	24.18	24.32	24.52	24.42	24.63	24.69	24.48	23.63	23.65	23.20	24.12	24.51	
Total	99.18	100.1	99.17	100.07	98.97	99.65	99.46	98.93	100.85	100.12	100.13	99.68	99.91	98.08	100.53	
	apfu															
Cd	0.77	0.82	0.78	0.82	0.78	0.80	0.81	0.75	0.72	0.74	0.85	0.89	0.87	0.80	0.77	
Zn	0.17	0.15	0.19	0.15	0.20	0.16	0.16	0.21	0.22	0.21	0.07	0.06	0.07	0.16	0.16	
Cu	0.03	0.00	0.01	0.00	0.00	0.00	0.00	0.00	0.04	0.03	0.05	0.02	0.04	0.01	0.04	
Fe	0.01	0.00	0.00	0.00	0.00	0.00	0.00	0.01	0.02	0.01	0.01	0.01	0.01	0.00	0.01	
Mn	0.00	0.00	0.00	0.00			0.00		0.00	0.00	0.00	0.00	0.00	0.00		
Ag									0.00	0.00	0.00	0.00	0.00	0.00		
S	1.02	1.03	1.02	1.02	1.02	1.03	1.03	1.03	1.00	1.01	1.01	1.02	1.00	1.03	1.01	
Cd/(Cd+Zn)	0.82	0.85	0.8	0.84	0.8	0.83	0.84	0.78	0.77	0.78	0.92	0.93	0.92	0.83	0.83	
	k31b.15								k31b.16							
Sample	2	3	4	5	6	7	8	1	2	3	4	5	6	7	8	
	wt %															
Cd	65.06	66.33	71.23	66.36	71.65	63.41	72.6	71.05	65.86	66.62	63.98	71.15	72.66	64.85	65.64	
Zn	9.09	7.57	3.57	7.63	2.66	10.37	2.97	4.10	8.17	8.51	9.83	4.29	3.00	8.32	8.02	
Cu	0.94	1.97	0.72	0.76	2.36	0.92	0.91	1.29	0.55	0.55	0.62	0.68	1.16	1.85	1.86	
Fe	0.18	0.38	0.11	0.30	0.36	0.23	0.28	0.32	0.27	0.21	0.46	0.32	0.26	0.76	0.46	
Mn	n/d	n/d	0.03	n/d	n/d	0.02	0.07	n/d	0.01	0.03	n/d	0.01	0.02	0.01	n/d	
Ag	0.07	0.04	0.04	0.01	0.04	n/d	n/d	n/d	n/d	0.03	0.07	0.02	n/d	n/d	0.08	
S	24.13	23.9	22.71	24.29	23.57	25.05	23.76	23.83	24.25	24.07	24.57	23.08	23.19	24.64	24.72	
Total	99.47	100.18	98.39	99.35	100.63	100.01	100.58	100.59	99.10	100.02	99.53	99.53	100.3	100.43	100.77	
	apfu															
Cd	0.78	0.79	0.90	0.80	0.88	0.74	0.89	0.86	0.79	0.80	0.76	0.88	0.90	0.76	0.77	
Zn	0.19	0.16	0.08	0.16	0.06	0.21	0.06	0.09	0.17	0.16	0.20	0.09	0.06	0.17	0.16	
Cu	0.02	0.04	0.02	0.02	0.05	0.02	0.02	0.03	0.01	0.01	0.01	0.02	0.03	0.04	0.04	
Fe	0.00	0.01	0.00	0.08	0.01	0.01	0.01	0.01	0.01	0.01	0.01	0.01	0.01	0.02	0.01	
Mn			0.00			0.00	0.00		0.00	0.00		0.00	0.00	0.00		
Ag	0.00	0.00	0.00	0.00	0.00				0.00	0.00		0.00	0.00		0.00	
S	1.01	1.00	1.01	1.02	1.01	1.03	1.02	1.02	1.02	1.01	1.02	1.00	1.01	1.01	1.02	
Cd/(Cd+Zn)	0.81	0.84	0.92	0.83	0.94	0.78	0.93	0.91	0.82	0.82	0.79	0.91	0.93	0.82	0.83	

4.2.2. Associated Minerals

Cobaltite, bornite, wittichenite, tetrahedrite, stannoidite, and sphalerite were also analyzed by EPMA. The results are provided in Tables 2 and 3. With the exception of Co, As, and S, the cobaltite contained minor Fe (0.46–1.28 wt %) and Ni (0.87–3.35 wt %), and all the As/S molar ratios were less than 1, ranging from 0.97 to 0.99, with the exception of three low values (0.62–0.69; Table 2). The bornite contained trace Bi (0.09–0.22 wt %), Ag (0.21–2.84 wt %), and Cd (0.02–0.03 wt %). The wittichenite contained minor Fe (0.39–0.74 wt %) and Ag (0.21–0.67 wt %), while the tetrahedrite contains minor Zn (5.06–5.11 wt %) and Ag (0.50–4.49 wt %), and trace Co (0.15–0.29 wt %). The sphalerite is Fe-poor (0.92–1.18 wt %), but Cd-rich (0.50–0.57 wt %; Table 3).

Table 2. Representative EPMA data and atomic proportions of cobaltite.

Sample	Fe	Co	Ni	As	S	Total	Fe	Co	Ni	As	S	As/S
	wt %					apfu						
1.2b	1.00	31.90	1.50	44.79	19.54	98.73	0.03	0.91	0.04	1.00	1.02	0.98
1.3	1.18	32.40	1.52	44.94	19.53	99.57	0.04	0.91	0.04	1.00	1.01	0.98
1.4	0.82	31.98	1.60	44.70	19.66	98.75	0.02	0.91	0.05	1.00	1.03	0.97
2.1	0.50	32.80	3.35	39.56	24.48	100.68	0.01	0.87	0.09	0.83	1.20	0.69
3.1	0.46	33.81	2.93	36.59	25.44	99.23	0.01	0.90	0.08	0.77	1.24	0.62
4.1	0.50	33.17	2.98	38.54	24.63	99.82	0.01	0.89	0.08	0.81	1.21	0.67
5.1	1.07	32.73	0.87	45.57	19.72	99.96	0.03	0.92	0.02	1.01	1.02	0.99
5.2	0.90	32.81	1.23	45.60	19.65	100.20	0.03	0.92	0.03	1.01	1.01	0.99
5.3	1.22	32.38	1.20	45.37	19.55	99.72	0.04	0.91	0.03	1.01	1.01	0.99
5.4	1.28	32.11	1.15	45.64	19.81	99.97	0.04	0.90	0.03	1.01	1.02	0.99
6.1	1.20	32.91	1.14	45.47	19.63	100.35	0.04	0.92	0.03	1.00	1.01	0.99

Table 3. Representative EPMA data for bornite, wittichenite, tetrahedrite, stannoidite, and sphalerite.

Sample	Bi	Ag	Cu	Co	Cd	Fe	Zn	Sb	As	Sn	S	Total	Bi	Ag	Cu	Co	Cd	Fe	Zn	Sb	As	Sn	S
	wt %												apfu										
Bornite													$\Sigma 10$ atoms										
bn6a.2	0.21	0.21	62.81	0.01	0.02	11.02	n/a	n/a	0.02	n/a	25.23	99.54	0.01	0.01	5.00	0.00	0.00	1.00			0.00		3.98
bn6a.1	0.09	0.24	63.55	0.05	0.02	10.44	n/a	n/a	0.07	n/a	24.81	99.26	0.00	0.01	5.09	0.00	0.00	0.95			0.00		3.94
bn1.1	0.22	2.84	60.51	0.04	0.03	11.18	n/a	n/a	0.08	n/a	24.59	99.48	0.01	0.14	4.89	0.00	0.00	1.03			0.01		3.94
Wittichenite													$\Sigma 7$ atoms										
lbt1.1	40.9	0.55	39.29	n/a	n/a	0.33	n/a	n/a	n/a	n/a	19.84	100.9	0.95	0.02	3.00			0.03					3.00
lbt2.1	40.8	0.42	39.63	n/a	n/a	0.39	n/a	n/a	n/a	n/a	19.80	101.04	0.94	0.02	3.02			0.03					2.99
lbt3.1	40.86	0.67	39.33	n/a	n/a	0.53	n/a	n/a	n/a	n/a	19.95	101.34	0.94	0.03	2.98			0.05					3.00
lbt4.1	40.48	0.24	39.3	n/a	n/a	0.74	n/a	n/a	n/a	n/a	19.57	100.32	0.94	0.01	3.01			0.06					2.97
lbt5.1	40.1	0.28	39.36	n/a	n/a	0.5	n/a	n/a	n/a	n/a	19.98	100.22	0.93	0.01	3.00			0.04					3.02
lbt6.1a	40.6	0.21	40.23	n/a	n/a	0.64	n/a	n/a	n/a	n/a	19.87	101.55	0.93	0.01	3.03			0.05					2.97
Tetrahedrite													$\Sigma 29$ atoms										
y6.1	2.97	0.63	39.79	0.22	1.67	0.41	5.11	14.2	7.96	n/a	24.98	97.93	0.24	0.10	10.36	0.06	0.25	0.12	1.29	1.93	1.76		12.89
y5.1	3.14	0.5	39.68	0.29	1.77	0.39	5.06	14.73	7.55	n/a	25.03	98.13	0.25	0.08	10.34	0.08	0.26	0.12	1.28	2.00	1.67		12.92
y2.1	4.55	4.49	37.99	0.15	0.88	0.2	5.06	15.11	6.33	n/a	24.82	99.57	0.36	0.70	9.99	0.04	0.13	0.06	1.29	2.07	1.41		12.94
Stannoidite													$\Sigma 12$ atoms										
3.4	n/a	0.02	38.11	0.21	0.05	10.89	2.47	n/a	n/a	17.95	28.44	98.15		0.00	3.84	0.02	0.00	1.25	0.24			0.97	5.68
3.5	n/a	0.09	38.12	0.2	0.03	10.51	2.86	n/a	n/a	17.72	28.27	97.79		0.01	3.86	0.02	0.00	1.21	0.28			0.96	5.67
3.5a	n/a	0.08	38.59	0.23	0	10.34	2.6	n/a	n/a	17.61	29.02	98.47		0.00	3.86	0.02	0.00	1.18	0.25			0.94	5.75
3.6	n/a	0.11	39.13	0.13	0	10.13	2.86	n/a	n/a	17.42	28.65	98.42		0.01	3.92	0.01	0.00	1.16	0.28			0.93	5.69
2a.3	n/a	0.2	37.84	0.2	0.04	10.74	2.8	n/a	n/a	17.66	29.07	98.55		0.01	3.78	0.02	0.00	1.22	0.27			0.94	5.75
Sphalerite													$\Sigma 2$ atoms										
3.3	0.1	n/d	0.1	n/a	0.56	1.07	65.73	n/a	n/a	n/a	32.09	99.65	0.00		0.00		0.00	0.02	0.99				0.99
3.2	0.03	n/d	0.07	n/a	0.5	1.12	65.39	n/a	n/a	n/a	32.02	99.13	0.00		0.00		0.00	0.02	0.99				0.99
3.1	0.01	n/d	0.06	n/a	0.55	0.92	66.24	n/a	n/a	n/a	31.58	99.36	0.00		0.00		0.00	0.02	1.00				0.98
2a.1	0.03	n/d	0.17	n/a	0.57	1.06	65.02	n/a	n/a	n/a	31.72	98.56	0.00		0.00		0.01	0.02	0.99				0.98
2a.2	0.06	n/d	0.1	n/a	0.56	1.18	65.66	n/a	n/a	n/a	32.13	99.68	0.00		0.00		0.00	0.02	0.99				0.99

4.3. XRD Data of Zinc Greenockite

The largest zinc greenockite grains (Figure 6f) were measured and the XRD patterns are indicated in Figure 10, while the peak data are provided in Table 4. The peak data patterns were in accordance with those of zincian greenockite from the International Centre for Diffraction Data (ICDD) PDF No. 40-0835, suggesting the zinc greenockite of the Saishitang deposit is hexagonal. In comparison to No. 40-0835, the unit-cell data of the zinc greenockite of the Saishitang deposit had a smaller a parameter, but a larger c parameter and cell volume V .

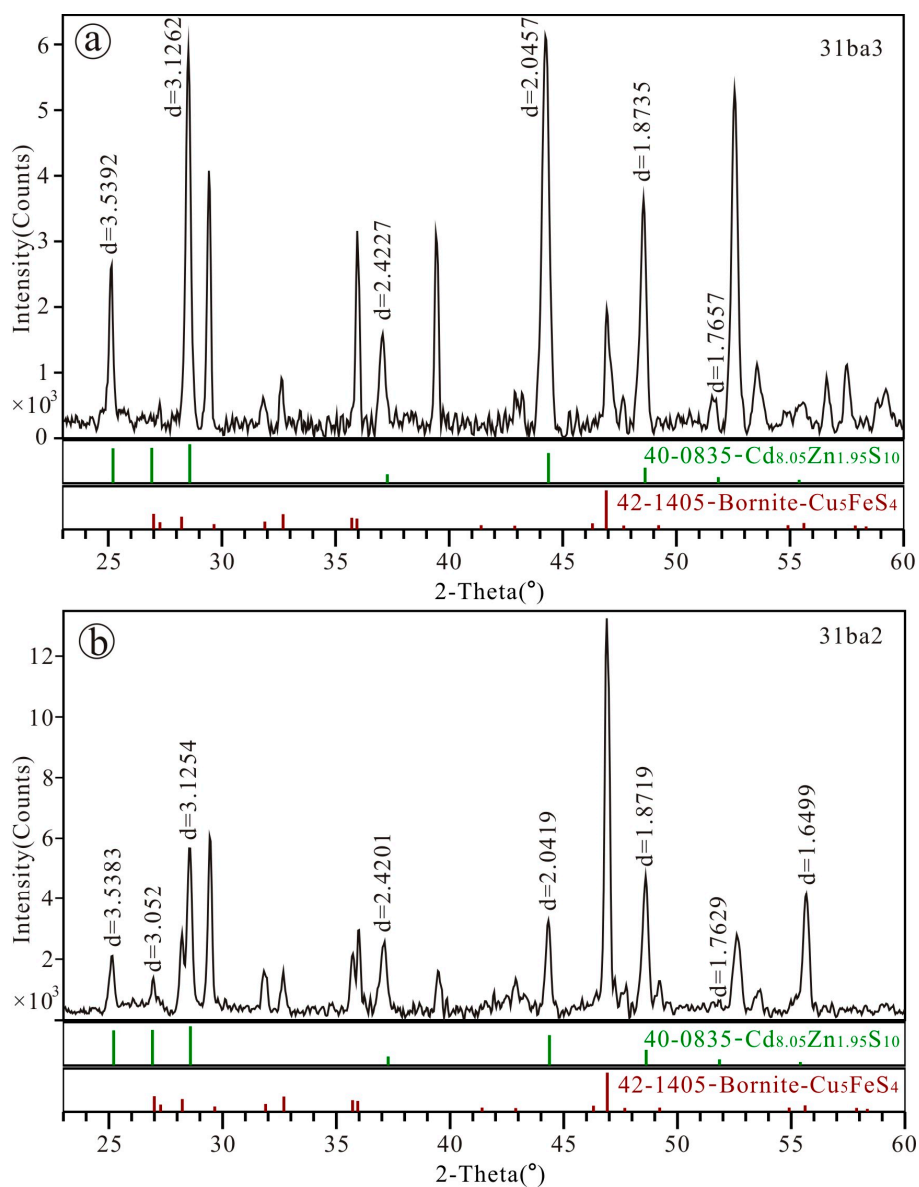


Figure 10. X-ray diffraction patterns of zincian greenockite from two analysis spots (a) spot 31ba3, and (b) spot 31ba2 (peak data listed in Table 4) with the corresponding the International Centre for Diffraction Data references.

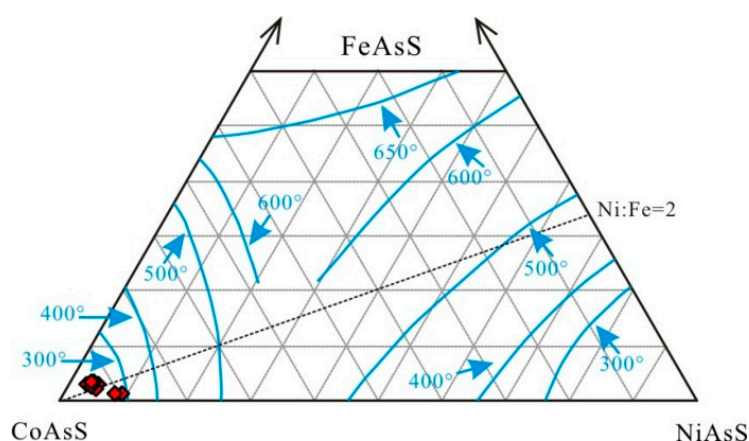
Table 4. X-ray diffraction data for zinc greenockite in comparison with ICDD data.

PDF#40-0835 (Cd _{8.05} Zn _{1.95})S ₁₀			31ba3		31ba2	
Hex			Hex		Hex	
hkl	d	I	d _{exp}	I _{est}	d _{exp}	I _{est}
100	3.530	89.0	3.5392	39.9	3.5383	33.6
002	3.310	90.0	3.3168	2.3	3.3052	20.7
101	3.120	100.0	3.1262	93.7	3.1254	100.0
102	2.410	18.0	2.4227	22.3	2.4201	43.9
110	2.040	76.0	2.0457	100.0	2.0419	53.9
103	1.871	36.0	1.8735	56.7	1.8719	77.0
200	1.762	10.0	1.7657	6.8	1.7629	4.3
004	1.657	3.0	1.6534	5.3	1.6499	71.1
<i>a</i> , Å	4.131(1)		4.086(5)		4.079(6)	
<i>c</i> , Å	6.173(5)		6.628(6)		6.618(5)	
<i>V</i> , Å ³	94.94		95.85		95.37	

5. Discussion

5.1. Factors Influencing Composition of Zincian Greenockite

The experimental and natural assemblage data indicated that the zincian greenockite composition was influenced by the chemical composition of the ore fluid (e.g., the Zn/Cd ratio and possibly Cl[−] content [4]) and the physicochemical parameters (pH, *f*S₂, *f*O₂, aH₂S) [4,7,42], of which temperature was most important. Fluid inclusion microthermometric data were obtained in previous studies [29,37,43]; however, the temperature of the sulfide-sulfosalt stage containing the zincian greenockite was not attained, due to the varying divisions of the different mineralization stages by different researchers [29,37,43]. The temperature of Stages IV to VI was found to be 235–366 °C by He et al. (2013) [43], while in Lu et al. (2016) it was 205–360 °C [29]. Zincian greenockite was thus formed between 205–360 °C. Furthermore, according to the mineral assessment, it appeared later than the cobaltite, but earlier than native silver and native bismuth. The cobaltite contained 0.46–1.28 wt % Fe, 31.90–33.81 wt % Co, and 0.87–2.98 wt % Ni, and plots in the area below 300 °C of the FeAsS-CoAsS-NiAsS figure (Figure 11) [44]. The melting point of native bismuth is 271 °C. Therefore, the zincian greenockite was formed under temperatures between 300 and 271 °C.

**Figure 11.** Compositions of cobaltite in the system of CoAsS-FeAsS-NiAsS, mol % (after [44]).

The EPMA data indicated that zincian greenockite contains 72.4–89.9 mol % CdS, which was in accordance with the experimental data of the ZnS-CdS system at 250 °C [7], and furthermore, the composition and structure were in line with the greenockite series [45] (cited in [2]). The Zn

content varied (5.61 to 21.7 mol % ZnS), similar to other occurrences of greenockite in hydrothermal deposits [4,11], e.g., 6–11 mol % ZnS in the Madjarovo Pb-Zn deposit [21], the maximum difference in different types of greenockite in the Caledonia Group being <1 to 25 mol % ZnS [11], and 42–59 mol % ZnS in the Tsumeb, southwest Africa [17]. In comparison to other occurrences, the zincian greenockite in the Saishitang deposit could be divided into two phases (I and II). Even within each phase, the composition was inhomogeneous, e.g., Phase I contained 14.6–21.7 mol % ZnS and 72.4–82.2 mol % CdS, while Phase II contained 5.6–9.1 mol % ZnS and 85.4–89.9 mol % CdS. The differences between two phases of zincian greenockite may have been the result of variation of fS_2 , fO_2 , T , Zn/Cd ratio during formation. Mineral assemblages and paragenetic sequences of the Stage VI that contained zincian greenockite were affected mainly by fS_2 ; thus, fS_2 was the key factor for the two phases.

Additionally, trace amounts of Cu and Sn can affect the chemical composition of greenockite, and the maximum Cu and Sn contents can reach 0.05 wt % [8,9]. The Cu content of zincian greenockite of the Saishitang deposit varied from 0.06 to 2.39 wt %, which may also be a factor influencing its composition.

5.2. Zincian Greenockite Formed during the Skarn Mineralization Processes

Evidence from both this study and previous research [28,29] suggest that the Saishitang deposit experienced skarn and hydrothermal processes. During initial magmatic-hydrothermal processes, fluids were oxidized and magnetite was precipitated, and iron orebodies were formed locally. Following this, the fluid reduced and sulfides (e.g., pyrrhotite, pyrite, cobaltite, bornite, and chalcopyrite) were formed, particularly bornite under low fS_2 fluids [3]; when the temperature decreased, sphalerite and galena were precipitated; and finally, during the sulfide-sulfosalt stage, oxidation of fluids occurred, and stromeyerite, zincian greenockite, and native silver and bismuth were formed. Thus the zincian greenockite was formed in a transforming environment from a reducing environment to an oxidizing one during the final stage of the mineralization process of the Saishitang Cu deposit.

The textural and mineral association of the zincian greenockite of the Saishitang deposit suggested that it is of hypogene origin. The greenockite may have been crystallized from low-Zn, high-Cd, late-stage hydrothermal fluids [11,21].

6. Conclusions

- (1) The zincian greenockite of the Saishitang skarn deposit occurs in the chalcopyrite-bornite ores and was formed during the sulfide-sulfosalt stage of the mineralization process. The chemical composition shows that it contains two phases (I and II). Phase I contains high Zn (14.6 to 21.7 mol % ZnS) and low Cd (72.4 to 82.2 mol % CdS), while Phase II contains low Zn (5.6 to 9.1 mol % ZnS) and high Cd (85.4 to 89.9 mol % CdS). The XRD data indicate that the zincian is hexagonal.
- (2) Zincian greenockite was formed at temperatures of 300–270 °C in a reducing to oxidizing environment during the late mineralization stage of the Saishitang skarn Cu deposit.

Acknowledgments: This work was jointly supported by the National Natural Science Foundation of China (Grant 41302048), the Innovation-driven Plan in Central South University (Grant 2015CX008), and a scholarship from China Scholarship Council (Grant 201406375045) for Jianping Liu to visit the University of Waterloo during 2015–2016. We thank Shoufa Lin of the University of Waterloo (Canada) and Stylianos Tombros of the University of Patras (Greece) for their valuable comments on a draft manuscript of this paper.

Author Contributions: Jianping Liu and Shugen Zhang conceived and designed the experiments; Jianping Liu performed the experiments; Jianping Liu and Shugen Zhang wrote the paper.

Conflicts of Interest: The authors declare no conflict of interest.

References

1. Chen, W.W.; Zhang, J.M.; Ardell, A.J.; Dunn, B. Solid state phase equilibria in the ZnS-CdS system. *Mater. Res. Bull.* **1988**, *23*, 1667–1673. [[CrossRef](#)]

2. Chaplygin, I.V.; Mozgova, N.N.; Mokhov, A.V.; Koporulina, E.V.; Bernhardt, H.J.; Bryzgalov, I.A. Minerals of the system ZnS-CdS from fumaroles of the Kudriavy volcano, Iturup island, Kuriles, Russia. *Can. Mineral.* **2007**, *45*, 709–722. [[CrossRef](#)]
3. Cook, N.J.; Ciobanu, C.L. Paragenesis of Cu-Fe ores from Ocna de Fier-Dognecea (Romania), typifying fluid plume mineralization in a proximal skarn setting. *Mineral. Mag.* **2001**, *65*, 351–372. [[CrossRef](#)]
4. Tombros, S.; Seymour, K.S.; Spry, P.G.; Williams-Jones, A. Greenockite and zincian greenockite in epithermal polymetallic Ag-Au-Te mineralization, Tinos Island, Hellas: Description and conditions of formation. *Neues Jahrb. Mineral. Abh.* **2005**, *182*, 1–9. [[CrossRef](#)]
5. Skinner, B.J.; Bethke, P.M. The relationship between unit-cell edges and compositions of synthetic wurtzites. *Am. Mineral.* **1961**, *46*, 1382–1398.
6. Cherin, P.; Lind, E.L.; Davis, E.A. The preparation and crystallography of cadmium zinc sulfide solid solutions. *J. Electrochem. Soc.* **1970**, *117*, 233–236. [[CrossRef](#)]
7. Tauson, V.L.; Chernyshev, L.V. Phase relationships and structural features of the ZnS-CdS mixed crystals. *Geochem. Int.* **1977**, *44*, 11–22.
8. Osadchii, E.G. Solid solutions and phase relations in the system $\text{Cu}_2\text{SnS}_3\text{-ZnS-CdS}$ at 850 °C and 700 °C. *Neues Jahrb. Mineral. Abh.* **1986**, *155*, 23–38.
9. Osadchii, E.G. The k esterite- ernyite and sphalerite-greenockite solid-solutions in the system $\text{Cu}_2\text{SnS}_3\text{-ZnS-CdS}$ at 400 °C and 101.3 MPa. *Neues Jahrb. Miner. Mon.* **1991**, *10*, 457–463.
10. Osadchii, E.G.; Lunin, S. Determination of activity-composition relations in $(\text{Fe}_x\text{Zn}_{1-x})$ solid solutions at 850–1020 K by solid state EMF measurements. *Exper. Geosci.* **1994**, *4*, 48–50.
11. Mogessie, A.; Gallien, F.; Bernhard, F.; Bauer, C.; Castro De Machuca, B.; Meissl, E.; Bjerg, E.; Delpino, S. Greenockite and associated sulfide mineralization from the Caledonia Group mines, Blanca Creek, La Huerta Range, San Juan province, Argentina. *Can. Mineral.* **2009**, *47*, 129–141. [[CrossRef](#)]
12. Mishra, B.; Hazarika, P. Rare greenockite (CdS) within the chromite-PGE association in the Bangur Gabbro, Baula-Nuasahi Complex, Eastern India. *Ore Geol. Rev.* **2016**, *72*, 1327–1334. [[CrossRef](#)]
13.  erny, P.; Harris, D.C. The Tanco pegmatite at Bernic Lake, Manitoba. XI. Native elements, alloys, sulfides and sulfosalts. *Can. Mineral.* **1978**, *16*, 625–640.
14. Butler, J.R.; Thompson, A.J. Cadmium and zinc in some alkali acidic rocks. *Geochim. Cosmochim. Acta* **1967**, *31*, 97–105. [[CrossRef](#)]
15. Burianova, E.Z. On the mineralogy and geochemistry of cadmium in sedimentary rocks. *Geokhimiya* **1960**, *2*, 177–182.
16. Davies, C.R.J.; Nelson, P.O.; Williamson, K.J. Sulfide control of cadmium and copper concentrations in anaerobic estuarine sediments. *Mar. Chem.* **1985**, *16*, 173–186. [[CrossRef](#)]
17. Hurlbut, S.C.J. The wurtzite-greenockite series. *Am. Mineral.* **1957**, *42*, 184–190.
18. Cornwall, H.B. Occurrence of greenockite on calcite from Joplin, Missouri. *Am. J. Sci.* **1902**, *14*, 7–8. [[CrossRef](#)]
19. Patterson, D.J. Zincian greenockite in stratiform lead-zinc-silver mineralization at Lady Loretta, northwest Queensland. *Can. Mineral.* **1985**, *23*, 89–94.
20. Oen, I.S.; Kager, P.; Kieft, C. Hawleyite and greenockite in ores from Los Blancos, Sierra de Cartagena, Spain. *Neues Jahrb. Miner. Mon.* **1974**, 507–513.
21. Tarkian, M.; Breskovska, V. Greenockite from the Madjarovo Pb-Zn ore district, eastern Rhodope, Bulgaria. *Mineral. Petrol.* **1989**, *40*, 137–144. [[CrossRef](#)]
22. Iizasa, K.; Yuasa, M.; Yokota, S. Mineralogy and geochemistry of volcanogenic sulfides from the Myojinsho submarine caldera, the Shichito-Iwojima Ridge, Izu-Ogasawara Arc, northwestern Pacific. *Mar. Geol.* **1992**, *108*, 39–58. [[CrossRef](#)]
23. Golding, L.Y. Mineralogy, Geochemistry and Origin of the Kalgoorlie Gold Deposits, Western Australia. Ph.D. Thesis, University of Melbourne, Melbourne, Australia, 1978.
24. Varas, G.; Menzies, A.; Peralta, A.; Sola, S.; Pizarro, H.; Sola, S.; Barraza, M. A rare occurrence of betekhtinite $[\text{Cu}_{10}(\text{Fe,Pb})\text{S}_6]$ and greenockite $[\text{CdS}]$ at La Platina deposit, Chile. In Proceedings of the XIV Congreso Geol gico Chileno, La Serena, Chile, 4–8 October 2015.
25. Fu, C.; Xiao, H.; Lang, K. *Geological Report on the Prospecting and Exploration of the Saishitang Deposit and Surrounding Area in Xinghai County, Qinghai Province*; The 3rd Geological Team of Qinghai Province: Xining, China, 1993. (In Chinese)

26. Liu, J.P.; Gu, X.P.; Shao, Y.J.; Feng, Y.Z.; Lai, J.Q. Indium mineralization in copper-tin stratiform skarn ores at the Saishitang-Rilonggou Ore Field, Qinghai, Northwest China. *Resour. Geol.* **2016**, *66*, 351–367. [[CrossRef](#)]
27. Li, F.; Zhang, H.; Song, Z.; Su, Z.; Liu, R.; Li, W. *The Ngola Shan Region Paleo-Thermal Mineralization Pattern*; Xi'an Jiaotong University Press: Xi'an, China, 1993. (In Chinese)
28. Wang, H.; Feng, C.Y.; Li, D.X.; Li, C.; Ding, T.Z.; Liao, F.Z. Geology, geochronology and geochemistry of the Saishitang Cu deposit, East Kunlun Mountains, NW China: Constraints on ore genesis and tectonic setting. *Ore Geol. Rev.* **2016**, *72*, 43–59. [[CrossRef](#)]
29. Lu, Y.C.; Liu, J.J.; Zhang, D.; Carranza, E.J.M.; Zhai, D.G.; Ge, L.S.; Sun, H.; Wang, B.; Chen, Y.F.; Liu, P. Genesis of the Saishitang skarn type copper deposit, west Qinling, Qinghai Province: Evidence from fluid inclusions and stable isotopes. *Ore Geol. Rev.* **2016**, *75*, 268–283. [[CrossRef](#)]
30. Mo, X.X.; Luo, Z.H.; Deng, J.F.; Yu, X.H.; Liu, C.D.; Chen, H.W.; Yuan, W.M.; Liu, Y.H. Granitoids and crustal growth in the east Kunlun orogenic belt. *Geosci. J. China Univ.* **2007**, *13*, 403–414. (In Chinese)
31. Dai, J.G.; Wang, C.S.; Hourigan, J.; Santosh, M. Multi-stage tectono-magmatic events of the Eastern Kunlun Range, northern Tibet: Insights from U-Pb geochronology and (U-Th)/He thermochronology. *Tectonophysics* **2013**, *599*, 97–106. [[CrossRef](#)]
32. Wang, B.Z.; Chen, J.; Luo, Z.H.; Chen, F.B.; Wang, T.; Guo, G.E. Spatial and temporal distribution of Late Permian-Early Jurassic intrusion assemblages in eastern Qimantag, East Kunlun, and their tectonic settings. *Acta Petrol. Sin.* **2014**, *30*, 3213–3228. (In Chinese)
33. Ma, L.F. *The Geological Atlas of China*; Geological Publishing House: Beijing, China, 2002. (In Chinese)
34. Li, W.L.; Xia, R.; Qing, M.; Li, C.; Zhang, D.; Sun, H.; Lu, Y.C.; Liu, P.; Zhou, A.B. Re-Os molybdenite ages of the Shenduolong skarn Mo-Pb-Zn deposit and geodynamic framework, Qinghai Province. *Rock Miner. Anal.* **2014**, *33*, 900–907. (In Chinese)
35. Song, Z.; Zhang, H.; Li, W.; Zhang, X.; Wang, W. Metallogenic conditions and model of copper multi-metal deposits in the Ngola Shan region. Qinghai Province. *Northwest Geosci.* **1995**, *16*, 134–144. (In Chinese)
36. Gu, X.P.; Xie, X.D.; Wu, X.B.; Zhu, G.C.; Lai, J.Q.; Hoshino, K.; Huang, J.W. Ferrisepiolite: A new mineral from Saishitang copper skarn deposit in Xinghai County, Qinghai Province, China. *Eur. J. Mineral.* **2013**, *25*, 177–186.
37. Lai, J.Q.; Ju, P.J.; Mao, Y.; An, J.H.; Wang, X.J. Ore-forming fluids characteristics of the Saishitang Cu-polymetallic deposit in Qinghai, China. *Acta Geol. Sin.* **2015**, *89*, 485–504.
38. Qiu, F.; Dong, J. Characters of magma and its mineralization in the Saishitang copper deposit in Qinghai Province. *Qinghai Geol.* **1978**, *1*, 1–19. (In Chinese)
39. Liu, J.P.; Lai, J.Q.; Gu, X.P.; Wang, X.J.; Mao, Y.; Song, W.B. Geochemistry and zircon LA-ICPMS U-Pb geochronology of intrusive body in Saishitang copper deposit, Qinghai Province, China. *Chin. J. Nonferrous Met.* **2012**, *22*, 622–632. (In Chinese)
40. Liu, Z.; Jiang, W.; Deng, A. *Geological Report on the Preliminary Exploration of the Saishitang Cu Deposit in Xinghai County, Qinghai Province*; The 3rd Geological Team of Qinghai Province: Xining, China, 1983. (In Chinese)
41. Wang, H.; Feng, C.Y.; Li, D.X.; Ding, T.Z.; Wang, H.Q.; Liu, J.N.; Zhou, J.H. Mineralogical characteristics and geological significance of skarn in the Saishitang copper deposit, Xinghai county, Qinghai Province. *Acta Geosci. Sin.* **2015**, *36*, 313–322. (In Chinese)
42. Wright, K.; Gale, J. Interatomic potentials for simulation of the zinc blende and wurtzite forms of ZnS and CdS: Bulk structure, properties, and phase stability. *Phys. Rev. B* **2004**, *70*, 35–41. [[CrossRef](#)]
43. He, P.; Yan, G.S.; Zhu, X.Y.; Zhang, Z.Y.; Wang, Y.L.; Cheng, X.Y.; Li, Y.S.; Zhen, S.M.; Du, Z.Z.; Jia, D.L.; et al. Fluid inclusion study of the Saishitang Cu deposit in Qinghai. *Geol. China* **2015**, *40*, 580–593. (In Chinese)
44. Klemm, D. Synthesen und Analysen in den Dreiecksdiagrammen FeAsS-CoAsS-NiAsS und FeS₂-CoS₂-NiS₂. *Neues Jahrb. Mineral. Abh.* **1965**, *103*, 205–255.
45. Tauson, V.L.; Chernyshov, L.V. *Experimental Study on Crystallochemistry and Geochemistry of Zinc Sulfide*; Nauka: Novosibirsk, Russia, 1981. (In Russian)

